

# Optoelectronic properties of ultrathin ALD silicon nitride and its potential as a hole-selective nanolayer for high efficiency solar cells

Cite as: APL Mater. 8, 111106 (2020); <https://doi.org/10.1063/5.0023336>

Submitted: 29 July 2020 . Accepted: 21 October 2020 . Published Online: 05 November 2020

 Edris Khorani, Shona McNab, Tudor E. Scheul,  Tasmia Rahman,  Ruy S. Bonilla, Stuart A. Boden, and Peter R. Wilshaw




View Online



Export Citation



CrossMark



additive manufacturing   epitaxial crystal growth   cerium oxide polishing powder   silver nanoparticles   sputtering targets   III-IV semiconductors   CVD precursors   europium phosphors

gallium lump   glassy carbon   nanodispersions   InAs wafers   laser crystals   ultra high purity materials   MOFs

surface functionalized nanoparticles   organometallics   quantum dot   rare earth metals   photovoltaics   refractory metals   MOCVD

superconductors   transparent ceramics   ultra high purity silicon

*American Elements opens up a world of possibilities so you can **Now Invent!***

Over 15,000 certified high purity laboratory chemicals, metals, & advanced materials and a state-of-the-art Research Center. Printable GHS-compliant Safety Data Sheets. Thousands of new products. And much more. All on a secure multi-language "Mobile Responsive" platform.

perovskite crystals   yttrium iron garnet   alternative energy   h-BN

gold nanocubes   graphene oxide   macromolecules   photonics

rhodium sponge   fiber optics   beamsplitters   infrared dyes   zeolites

fused quartz   metallocenes   platinum ink   buckyballs   Ti-6Al-4V

**Now Invent.**<sup>™</sup>

The Next Generation of Material Science Catalogs

[www.americanelements.com](http://www.americanelements.com)

# Optoelectronic properties of ultrathin ALD silicon nitride and its potential as a hole-selective nanolayer for high efficiency solar cells

Cite as: APL Mater. 8, 111106 (2020); doi: 10.1063/5.0023336

Submitted: 29 July 2020 • Accepted: 21 October 2020 •

Published Online: 5 November 2020



Edris Khorani,<sup>1,a)</sup> Shona McNab,<sup>2</sup> Tudor E. Scheul,<sup>1</sup> Tasmia Rahman,<sup>1</sup> Ruy S. Bonilla,<sup>2</sup> Stuart A. Boden,<sup>1</sup> and Peter R. Wilshaw<sup>2</sup>

## AFFILIATIONS

<sup>1</sup>School of Electronics and Computer Science, University of Southampton, SO17 1BJ Southampton, United Kingdom

<sup>2</sup>Department of Materials, University of Oxford, OX1 3PH Oxford, United Kingdom

<sup>a)</sup> Author to whom correspondence should be addressed: E.Khorani@soton.ac.uk

## ABSTRACT

Fully exploiting the power conversion efficiency limit of silicon solar cells requires the use of passivating contacts that minimize electrical losses at metal/silicon interfaces. An efficient hole-selective passivating contact remains one of the key challenges for this technology to be deployed industrially and to pave the way for adoption in tandem configurations. Here, we report the first account of silicon nitride ( $\text{SiN}_x$ ) nanolayers with electronic properties suitable for effective hole-selective contacts. We use x-ray photoemission methods to investigate ultrathin  $\text{SiN}_x$  grown via atomic layer deposition, and we find that the band alignment determined at the  $\text{SiN}_x/\text{Si}$  interface favors hole transport. A band offset ratio,  $\Delta E_C/\Delta E_V$ , of  $1.62 \pm 0.24$  is found at the  $\text{SiN}_x/\text{Si}$  interface for the as-grown films. This equates to a 500-fold increase in tunneling selectivity for holes over electrons, for a film thickness of 3 nm. However, the thickness of such films increases by 2 Å–5 Å within 48 h in cleanroom conditions, which leads to a reduction in hole-selectivity. X-ray photoelectron spectroscopy depth profiling has shown this film growth to be linked to oxidation, and furthermore, it alters the  $\Delta E_C/\Delta E_V$  ratio to  $1.22 \pm 0.18$ . The  $\text{SiN}_x/\text{Si}$  interface band alignment makes  $\text{SiN}_x$  nanolayers a promising architecture to achieve widely sought hole-selective passivating contacts for high efficiency silicon solar cells.

© 2020 Author(s). All article content, except where otherwise noted, is licensed under a Creative Commons Attribution (CC BY) license (<http://creativecommons.org/licenses/by/4.0/>). <https://doi.org/10.1063/5.0023336>

## I. INTRODUCTION

The need for renewable energy sources is ever increasing due to the immense pressure put on reserves of fossil fuels by our growing energy demands, as well as the environmental detriment from using these non-renewable counterparts. Among all renewable energy sources, photovoltaic (PV) technologies have shown great promise toward tackling such demands. This is primarily due to the abundance of solar energy and the rapid development and deployment of such technologies.<sup>1,2</sup> Currently, crystalline silicon comprises over 90% of the market share, and the PV community continues to strive toward reaching the power conversion efficiency (PCE) limit of this technology.<sup>1</sup> The bulk of this market is dominated by architectures that suffer from high electrical losses at the metal–Si interface, limiting these technologies to PCEs considerably lower than the

theoretical limit of 29.4%.<sup>3,4</sup> This arises from the high density of electronically active states at the metal/Si interface, which increases the trap-assisted Shockley–Read–Hall recombination of photogenerated carriers. Attempts to mitigate this loss using highly doped regions at the contacts enhance the loss of carriers via Auger recombination, which further limits the overall performance. Currently, the silicon PV industry is striving toward the Shockley–Queisser PCE limit by adopting novel passivating and selective contact technologies.<sup>5,6</sup> Regardless of the cell architecture, the pathway to achieving higher performance silicon solar cells is to passivate the contacted regions of the device.<sup>7–9</sup>

Passivating contacts incorporate a thin film between the silicon absorber and the metal contact. This architecture can simultaneously provide charge carrier selectivity and suppress recombination at this interface, resulting in a higher carrier

collection efficiency.<sup>9,10</sup> Ideally, a good passivating contact suppresses the electrical losses at the interface while maintaining a low resistivity.<sup>9,11</sup> Devices require passivation of both electron and hole contacts in order to reach PCEs exceeding 25%.<sup>9</sup> Commonly, silicon dioxide and phosphorous-doped hydrogenated amorphous silicon are used as electron-selective passivating contacts. The inherent silicon surface passivation ability and the favorable interfacial band alignments on crystalline silicon make these materials highly suitable. However, using SiO<sub>2</sub> for hole contacts has not reached the same high efficiencies.<sup>12–14</sup> Work into alternative structures for hole contacts is an important area of research.<sup>15,16</sup> Despite the advancements seen with electron-selective contacts, an efficient hole-selective passivating contact remains a key sought-after development to be accomplished in this industry.<sup>9</sup> To date, the most promising material candidates have been *p*-type amorphous silicon and silicon-rich silicon carbide, but compatibility with conventional high temperature Ag screen printing still remains an issue.<sup>5,13</sup>

Silicon nitride (SiN<sub>x</sub>) is renowned for its superior silicon surface passivation ability.<sup>17,18</sup> The semi-continuum of forbidden energy states that arise at the surfaces in a solar cell are known to be well saturated by silicon nitride. The use of this material as an anti-reflection, surface passivating layer has led to studies on the interface between SiN<sub>x</sub>/Si. This material is known to be compatible with conventional Ag screen print metallization. The density of interface states at this interface is commonly reported in the 10<sup>11</sup> cm<sup>-2</sup> to 10<sup>12</sup> cm<sup>-2</sup> region, with the recombination velocity generally lower than 1 cm s<sup>-1</sup>.<sup>19,20</sup> Incorporating an oxide or oxynitride layer can prove beneficial by offering a lower density of states that complements the SiN<sub>x</sub> layers low surface recombination.<sup>21</sup> Furthermore, previous theoretical calculations for the band offsets at an Si<sub>3</sub>N<sub>4</sub>/Si interface show hole transport being favorable, with a 28% larger barrier to electron tunneling than that for holes, determined from a calculated  $\Delta E_C/\Delta E_V$  factor of 1.28.<sup>22</sup> Despite these promising attributes toward hole-selective contacts, previous reports have suggested that PECVD nitride is not a viable option for hole tunneling due to the fixed positive charges that would create an inversion layer.<sup>23,24</sup> To date, no report exists on whether these charges form during processing, their potential to cause inversion in a thin layer, or the empirical values of band alignment at the Si<sub>3</sub>N<sub>4</sub>/Si interface.

We report the first experimental study of the optoelectronic properties of silicon nitride nanolayers and their potential as hole-selective contacts in silicon solar cells. We use bis(tertiary-butyl-amino)silane (BTBAS) to grow ultra-thin SiN<sub>x</sub> films via atomic layer deposition (ALD), following on from work by Knoops *et al.*<sup>25</sup> We then use x-ray photoelectron spectroscopy (XPS) to probe the electronic core levels (CLs) and states<sup>26</sup> at the SiN<sub>x</sub>/Si interface to experimentally determine the band alignments. This characterization has shown the potential for carrier selectivity of SiN<sub>x</sub>, thus corroborating theoretical predictions. Furthermore, we explore the effect of degradation over time on the band offsets at the SiN<sub>x</sub>/Si interface by probing and profiling the chemical states as a function of depth using XPS. In addition, we study the specific contact resistivity at various SiN<sub>x</sub> thicknesses using Au front and rear electrodes. Finally, we provide device simulations implementing a non-local tunneling method to calculate the improved tunneling of holes when SiN<sub>x</sub> nanolayers are used in silicon devices. Beyond the work reported here, full deployment as hole-selective passivating contacts still requires

maintaining superior Si surface passivation with such ultra-thin films, relative to its non-passivating counterparts.

## II. EXPERIMENTAL SECTION

### A. Specimen fabrication

The ALD process for each cycle of SiN<sub>x</sub> growth is comprised of two half-cycle reactions: (a) the precursor (BTBAS) half-cycle reaction and (b) nitrogen reactant half-cycle reaction. The first half-cycle consists of the chemisorption of precursor molecules onto the surface, followed by a purging step to remove excess molecules. The second half-cycle uses the nitrogen plasma to remove the unwanted surface ligands and form silicon–nitrogen bonds, followed by a purge to remove undesirable by-products. For this process, the chamber pressure was kept at 5 Pa, the plasma power at 400 W, and the bottom plate temperature at 350 °C. The film growth rate and the variation in the growth per cycle (GPC) were determined using different BTBAS dosing times (25 ms–225 ms) and different film thicknesses, grown on *p*-type Si (Cz, 1 Ω cm–10 Ω cm, ⟨100⟩, 300 μm) substrates and measured using spectroscopic ellipsometry. For optical bandgap determination, 10 nm and 25 nm of SiN<sub>x</sub> were grown on clear glass substrates that were ultrasonically cleaned in acetone and then rinsed in deionized water. For XPS measurements, 3 nm, 10 nm, and 25 nm thick SiN<sub>x</sub> films were grown on *p*-type Si (100) substrates that were immersed in buffered HF solution for native oxide removal prior to SiN<sub>x</sub> growth. A schematic representation of our process is shown in Fig. 1. The study of degradation from aging was carried out on several SiN<sub>x</sub> samples that were spin-coated with S1813 photoresist at 5000 rpm for 30 s and baked at 115 °C for 1 min. Photoresist was rinsed off using acetone and isopropanol immediately prior to each spectroscopic ellipsometry measurement during the degradation study. For specific contact resistivity measurements, we use photolithography to form circular patterns between 1 mm and 2 mm in diameter on *p*-Si substrates. SiN<sub>x</sub> layers with thicknesses between 1 nm and 4 nm are deposited in the openings, with another lithography step used to form the Au electrodes via E-beam evaporation.

SiN<sub>x</sub> films were grown in an Oxford Instruments Flex-AL Plasma Enhanced-ALD chamber. Spatial film thickness scans were taken using a M-2000 J.A. Woollam ellipsometer. For Au electrode formation, a Balzers BAK600 chamber is used. A Jasco V-750 UV–Visible (UV–Vis) spectrophotometer was used for transmission measurements to determine bandgap energy. A Thermo Scientific Theta Probe XPS system was used for the determination of core levels (CLs) and valence band maxima (VBM) of the grown films. This was done using a monochromatic Al Kα x-ray (1.487 keV) source with the same geometry used for emission in all measurements. Since the incident x-ray energy is lower than 1.5 keV, the photoelectron kinetic energy is lower than 1.5 keV, which results in a shallow escape depth (between 3 nm and 5 nm) for photoelectrons.<sup>27</sup> Depth profiles are conducted by milling away the material using an Ar ion gun with a current density of 1 μA mm<sup>-2</sup> and a raster area of 4 mm<sup>2</sup>.

### B. Band offset determination

The x-ray photoemission-based method proposed by Kraut,<sup>28,29</sup> and widely reported in the literature,<sup>30–33</sup> uses XPS spectra to

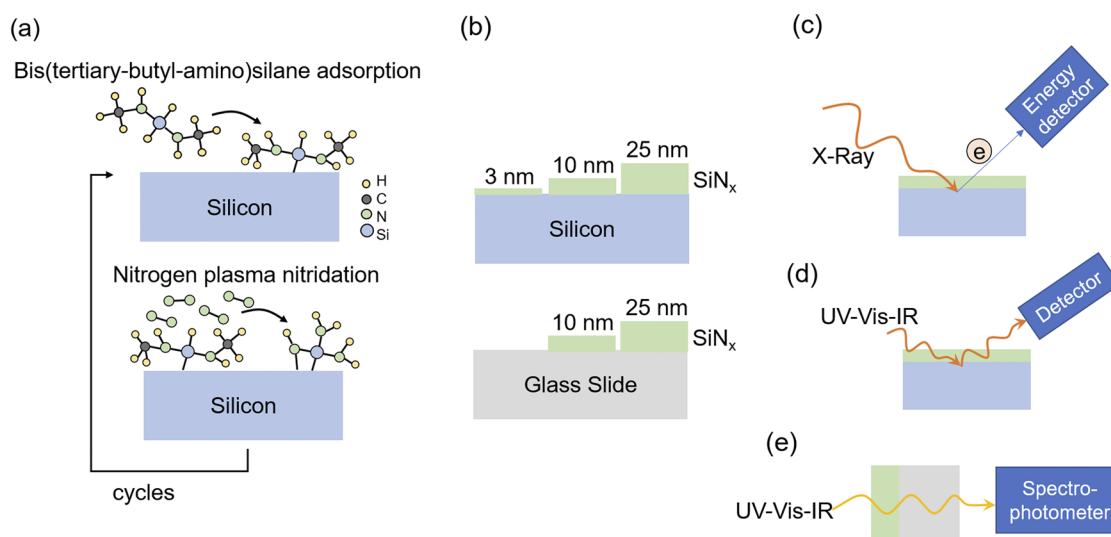


**FIG. 1.** Schematic diagram illustrating (a) the cyclic growth of  $\text{SiN}_x$  via atomic layer deposition forming (b) sample structures of interest for (c) x-ray photoelectron spectroscopy, (d) spectroscopic ellipsometry, and (e) transmittance spectroscopy measurements.

determine the valence band offset ( $\Delta E_V$ ) and conduction band offset ( $\Delta E_C$ ) energies at a semiconductor interface. This method utilizes Poisson's equation to predict these offsets based on the deviations in charge distribution found at the interface relative to the semiconductor bulk.<sup>28</sup> In this approach, the binding-energy difference between the electronic core level energy ( $E_{CL}$ ) and VBM are determined experimentally and used in Kraut's formulas to calculate  $\Delta E_V$  and  $\Delta E_C$ . A schematic band diagram at the  $\text{SiN}_x/\text{Si}$  interface that illustrates  $\Delta E_V$  and  $\Delta E_C$  from these calculations is shown in Fig. 2.

The valence band offset at the SiN<sub>x</sub>/(*p*)-Si interface was calculated using

$$\Delta E_V = (E_{CL}^{Si} - E_{CL}^{SiN_x})_{SiN_x/Si} - (E_{CL}^{Si} - E_V^{Si})_{Si} + (E_{CL}^{SiN_x} - E_V^{SiN_x})_{SiN_x}. \quad (1)$$

Here,  $(E_{\text{CL}}^{\text{Si}} - E_{\text{CL}}^{\text{SiN}_x})_{\text{SiN}_x/\text{Si}}$  is the energy difference between the CLs of the two materials at the interface, also known as  $\Delta E_{\text{CL}}$ . To probe the interface and determine  $\Delta E_{\text{CL}}$ , a 3 nm  $\text{SiN}_x$  film on a Si substrate was studied, based on the XPS photoelectron escape depth being under 5 nm. The energy difference between the core level centroids and valence band edges for Si  $(E_{\text{CL}}^{\text{Si}} - E_{\text{V}}^{\text{Si}})_{\text{Si}}$  and  $\text{SiN}_x$   $(E_{\text{CL}}^{\text{SiN}_x} - E_{\text{V}}^{\text{SiN}_x})_{\text{SiN}_x}$  were obtained from XPS of the respective thick films.  $\text{SiN}_x$  films with thicknesses of 25 nm and 10 nm were examined as independent bulk films in this study. The N 1s and Si 2p orbital peaks were used as  $E_{\text{CL}}^{\text{SiN}_x}$  and  $E_{\text{CL}}^{\text{Si}}$ , respectively. Linear extrapolation of the leading edge to the baseline of the valence band spectra from the respective thick films was used to obtain  $E_{\text{V}}^{\text{Si}}$  and  $E_{\text{V}}^{\text{SiN}_x}$ .<sup>30</sup> This method is widely reported as an accurate way of determining the VBM of semiconductors, assuming the use of high-precision (>0.1 eV) XPS.

Following Kraut's method,  $\Delta E_C$  was also determined using

$$\Delta E_C = \Delta E_V - (\Delta E_g)_{\text{Si-SiN}_x}, \quad (2)$$

where  $(\Delta E_g)_{\text{Si-SiN}_x}$  is the energy difference between the bandgap of Si and SiN<sub>x</sub> films, i.e.,  $E_g^{\text{Si}} - E_g^{\text{SiN}_x}$ . An energy gap of  $1.12 \pm 0.01$  eV was used as  $E_g^{\text{Si}}$  for these calculations.  $E_g^{\text{SiN}_x}$  was determined from

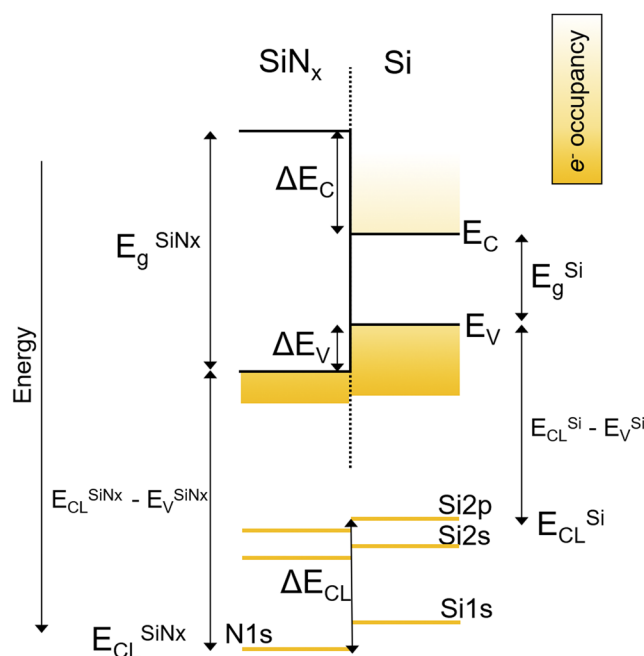


**FIG. 2.** Schematic diagram of band offsets at the SiN<sub>x</sub>/Si interface.

the absorption edge taken from UV–Vis transmission spectra using the Tauc method.<sup>34,35</sup>

### III. RESULTS AND DISCUSSION

#### A. Nanolayer growth dynamics

The growth per cycle (GPC) as a function of precursor dosing time is presented in Fig. 3(a). This is conducted by growing SiN<sub>x</sub> films with different thicknesses (i.e., range of ALD cycles) at a fixed BTBAS dosing time. The relationship between GPC and dosing time can be interpreted as softly saturating, whereby GPC is seen to increase with BTBAS dosing time, but with some indication that the GPC is saturating at higher dosing times. The relationship between GPC and BTBAS dosing time matches well with the findings of Knoops *et al.*,<sup>25</sup> despite some minor differences in the film growth recipe.

The relatively low growth rate is suggested to be due to the incomplete reaction of N<sub>2</sub> plasma with the *tert*-butyl groups of BTBAS. Furthermore, the non-uniform nucleation on the surface of the underlying substrate in the early cycles further reduces this growth rate. The schematic of the SiN<sub>x</sub> ALD cycle shown in Fig. 1

assumes uniform nucleation and surface reactions, which is unlikely to occur in the first few monolayers of growth. SiN<sub>x</sub> film growth at a fixed dosing time of 150 ms shows a linear increase in film thickness with the number of cycles [Fig. 3(b)]. The growth rate can be determined using the gradient of the fitted line, indicating a rate of 0.12 Å/cycle. This relatively slow growth rate is useful for accurately growing ultra-thin films for use as selective contacts, where differences in film thickness at an Å scale can cause significant variations in device performance.

#### B. Optical and electronic properties

The transmission spectra for 10 nm and 25 nm thick SiN<sub>x</sub> films are presented in Fig. 4(a). The region of interest in the transmission spectra is the inflection point, corresponding to  $h\nu \geq E_g$ . An abrupt absorption edge at ~320 nm is seen, which can give some indication to  $E_g^{\text{SiN}_x}$ . Figure 4(b) shows the Tauc plots for the 10 nm and 25 nm thick SiN<sub>x</sub> films. The optical bandgap is determined by extrapolating the linear region of the absorption edge to the baseline.<sup>32,36</sup> Using this method, an optical bandgap of  $3.98 \pm 0.04$  eV for this material is determined.

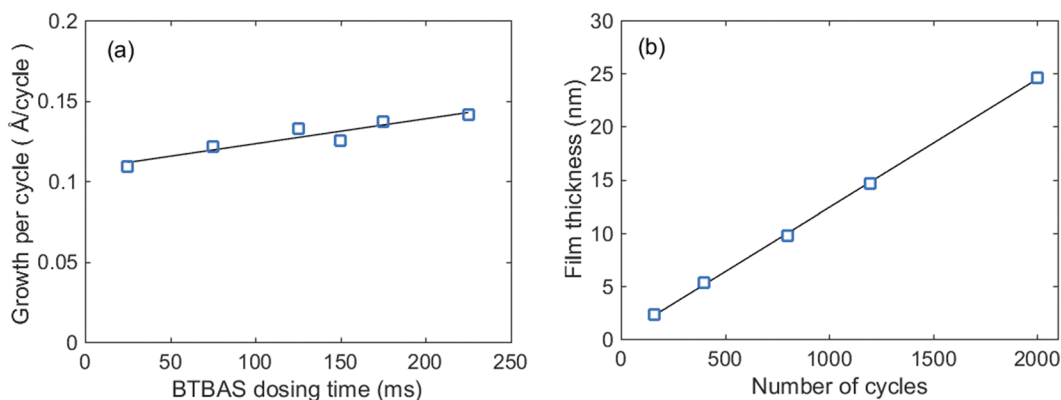


FIG. 3. (a) Growth per cycle as a function of BTBAS dosing time and (b) film thickness as a function of the number of cycles grown at a dosing time of 150 ms.

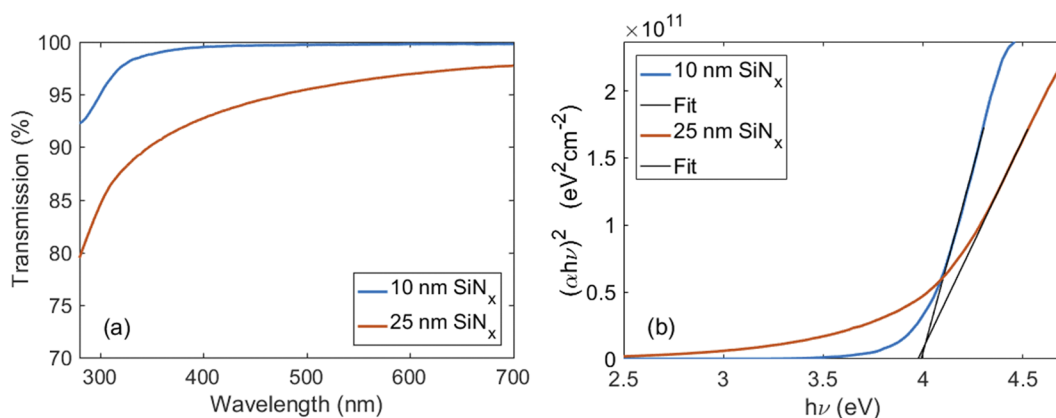
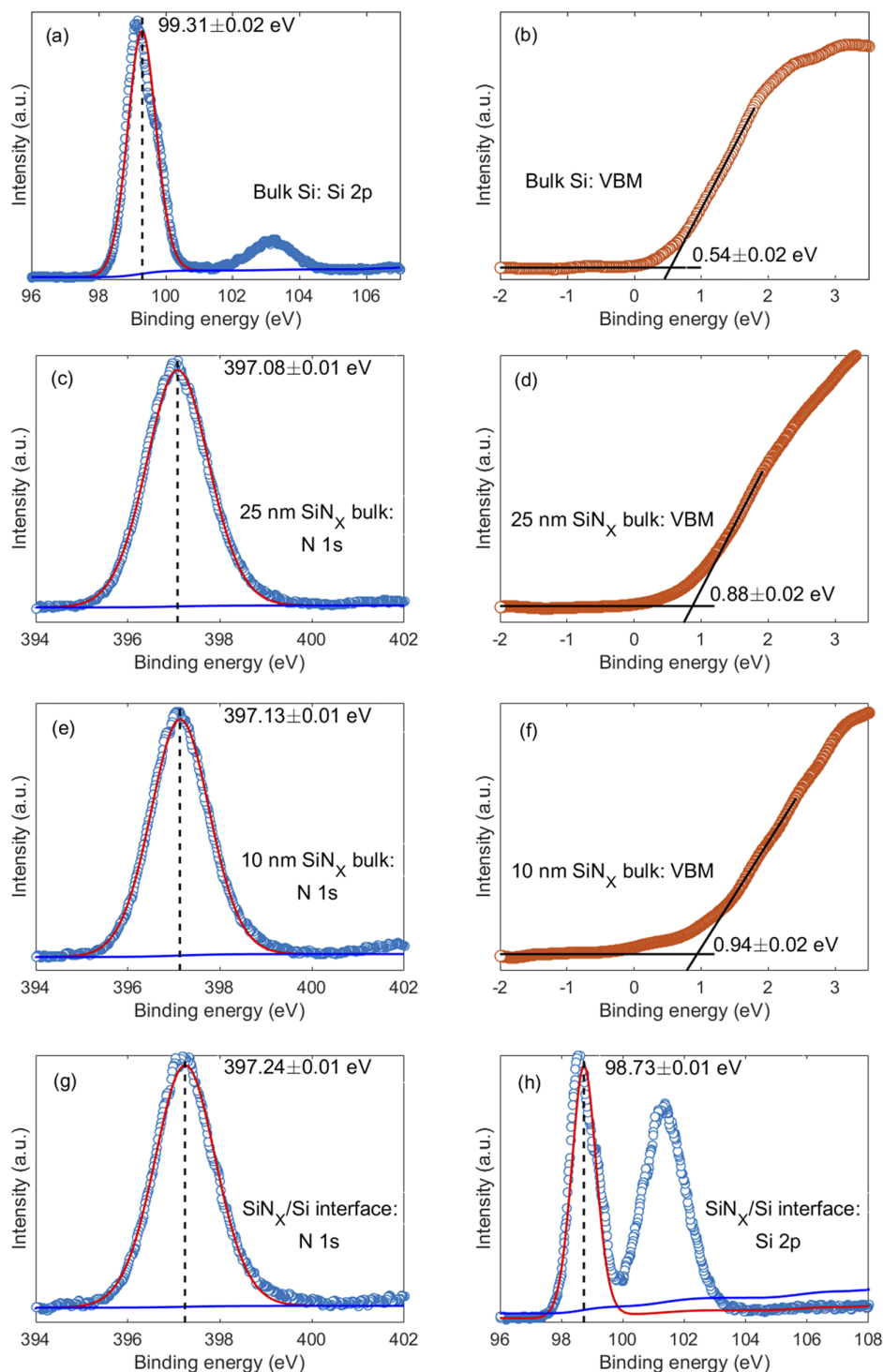


FIG. 4. (a) Transmission spectra and (b) Tauc  $[(\alpha h\nu)^2 \text{ vs } h\nu]$  plot for 10 nm and 25 nm SiN<sub>x</sub> films.

XPS spectra showing core level energy centroids and valence band edges for bulk Si, 25 nm  $\text{SiN}_x$  and 10 nm  $\text{SiN}_x$ , as well as the CLs at the (3 nm)  $\text{SiN}_x$ /Si interface are shown in Fig. 5. The CL positions did not change with x-ray irradiation time, and all XPS spectra

are calibrated to the C 1s peak at 284.8 eV. A Savitsky–Golay filter is used to fit all valence band edge spectra to a polynomial using the least squares method,<sup>37</sup> and all core level peaks are fitted using Shirley backgrounds and Voigt functions.<sup>33</sup> From Figs. 5(a) and 5(b),



**FIG. 5.** XPS spectra showing (a) Si 2p CL and (b) valence band edge from bulk *p*-type Si, (c) N 1s CL and (d) valence band edge from 25 nm (bulk)  $\text{SiN}_x$ , (e) N 1s CL and (f) valence band edge from 10 nm (bulk)  $\text{SiN}_x$ , and (g) N 1s CL and (h) Si 2p CL from 3 nm (interface)  $\text{SiN}_x$  on *p*-type Si. Red solid lines show Voigt fits, blue solid lines show the Shirley background, black dashed lines show the CL centroid positions [in (a), (c), (e), (g), and (h)], and black solid lines show the extrapolations to determine the VB edge [in (b), (d), and (f)].

the Si 2*p* core level energy and the leading edge of the valence band spectra for bare *p*-type Si are determined to be  $99.31 \pm 0.01$  eV and  $0.54 \pm 0.02$  eV, respectively. This suggests an energy difference of  $98.77 \pm 0.03$  eV for  $(E_{\text{Si}2p} - E_V)_{\text{Si}}$ , which is in agreement with findings in the literature.<sup>30,32</sup> Figures 5(c) and 5(d) show the N 1*s* core level energy and leading edge of the valence band spectra for the 25 nm thick films. The N 1*s* core level energy is detected at  $397.08 \pm 0.01$  eV and the valence band edge at  $0.88 \pm 0.02$  eV. Figures 5(e) and 5(f) show the N 1*s* core level energy and leading edge of the valence band spectra for the 10 nm thick films. The N 1*s* core level energy is detected at  $397.13 \pm 0.01$  eV and the valence band edge at  $0.94 \pm 0.02$  eV. Hence, an energy difference of  $396.20 \pm 0.03$  eV and  $396.19 \pm 0.03$  eV for  $(E_{\text{N}1s} - E_V)_{\text{SiN}_x}$  using the 25 nm and 10 nm specimen as bulk SiN<sub>x</sub> is determined. The core level energy peaks for SiN<sub>x</sub> (N 1*s*) and Si (Si 2*p*) at the interface from the 3 nm thick SiN<sub>x</sub> specimen are shown in Figs. 5(g) and 5(h). In Fig. 5(h), two peaks are seen for the Si 2*p* core level at the interface. This is because the Si 2*p* core level at the interface has contributions from both the substrate and the ultra-thin SiN<sub>x</sub> layer. As the thickness of the 3 nm SiN<sub>x</sub> layer is less than the x-ray penetration depth and the photoelectron escape depth, Si 2*p* electrons from both the SiN<sub>x</sub> and Si bulk layers are detected, resulting in a convoluted core level peak. Based on the ALSCOF XPS peak fitting library, the Si 2*p* peaks found closest to 101.30 eV and 99.4 eV are known to be due to nitrides and elemental silicon, respectively. Therefore, by de-convoluting the Si 2*p* peak in Fig. 5(h), the core level energy at the interface of Si ( $E_{\text{Si}2p}^{\text{Si}}$ )<sub>SiN<sub>x</sub>/Si</sub> is determined as  $98.73 \pm 0.01$  eV. To complete the Kraut calculation for this study, the SiN<sub>x</sub> ( $E_{\text{N}1s}^{\text{SiN}_x}$ )<sub>SiN<sub>x</sub>/Si</sub> core level energy is determined as  $397.24 \pm 0.01$  eV, resulting in an energy difference between these core levels at  $-298.51 \pm 0.03$  eV.

The valence band offset at the SiN<sub>x</sub>/Si interface is determined as  $-1.08 \pm 0.08$  eV and  $-1.09 \pm 0.08$  eV using the 25 nm and 10 nm thick SiN<sub>x</sub> films as bulk SiN<sub>x</sub>, respectively. A negative band offset value suggests that the valence band energy of SiN<sub>x</sub> is at a greater energy relative to the vacuum than the valence band energy of Si. From these  $\Delta E_V$  values and using the optical bandgap of the two bulk materials, the conduction band offset is determined as  $1.78 \pm 0.13$  eV and  $1.77 \pm 0.13$  eV. From these calculations,  $\Delta E_C/\Delta E_V$  ratios of  $1.64 \pm 0.24$  and  $1.62 \pm 0.24$  are established, suggesting favorability toward hole transport at this interface. The values calculated for both bulk SiN<sub>x</sub> films (10 nm and 25 nm thicknesses) are understandably in close agreement (and within the experimental uncertainty). Based on the  $\Delta E_C/\Delta E_V$  ratios, a lower tunneling potential barrier is defined for holes than for electrons. Despite showing favorability toward hole transport as-deposited, it is important to examine the stability of the films by studying how band offsets change over time.

### C. Understanding nanolayer degradation

To understand the impact of aging on these films when stored under different conditions, 3 nm SiN<sub>x</sub> films grown on Si were stored in our cleanroom within a desiccator, both with and without photoresist, over a two-week period. During this time, film thickness was repeatedly measured by spectroscopic ellipsometry, the results from which are plotted in Fig. 6. The thickness of all SiN<sub>x</sub> films studied is shown to increase over time, with no significant difference observed between storing in a desiccator or cleanroom. Thickness alterations

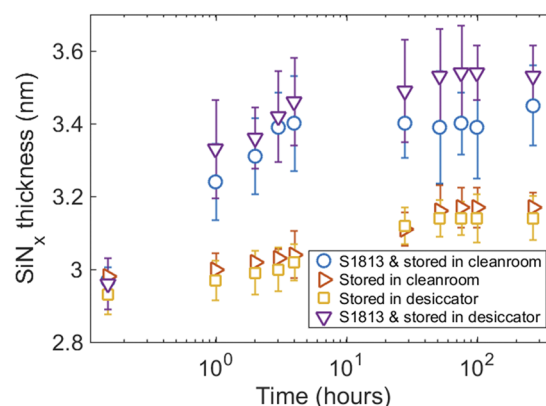


**FIG. 6.** SiN<sub>x</sub> thickness measured over two weeks when stored in a cleanroom and desiccator with and without the S1813 photoresist protection layer.

cease within the first 48 h. Films without photoresist protection are shown to increase in thickness by  $\sim 0.2$  nm, whereas the photoresist protected samples are shown to increase by  $\sim 0.5$  nm. This can be attributed to either remnants of photoresist after rinsing with acetone and isopropanol prior to each thickness measurement or due to alterations caused during the baking step after photoresist spinning.

Quantifying the impact of aging on the hole-selectivity of this film is crucial. Spectra and calculations presented for determining the band offsets in Sec. III B were all conducted immediately after film growth. Identical XPS measurements were conducted on these films after they were stored in the cleanroom for 1 week. The core levels and valence band edges for 25 nm and 10 nm thick SiN<sub>x</sub> and the core levels detected at the SiN<sub>x</sub>/Si interface after aging can be found in the [supplementary material](#). The N 1*s* core level energy and leading edge of the valence band spectra for the 25 nm thick films are detected at  $397.47 \pm 0.01$  eV and  $1.34 \pm 0.02$  eV, respectively. The N 1*s* core level energy and valence band spectra for the 10 nm thick film are detected at  $397.51 \pm 0.01$  eV and  $1.37 \pm 0.02$  eV, respectively. Therefore, this suggests an energy difference  $(E_{\text{N}1s} - E_V)_{\text{SiN}_x}$  of  $396.13 \pm 0.03$  eV and  $396.14 \pm 0.03$  eV after degradation, using the 25 nm and 10 nm specimen as bulk SiN<sub>x</sub>. The core level energy peaks ( $E_{\text{N}1s}^{\text{SiN}_x}$  and  $E_{\text{Si}2p}^{\text{Si}}$ ) at the interface are determined as  $397.45 \pm 0.01$  eV and  $98.79 \pm 0.01$  eV, respectively, resulting in  $\Delta E_{\text{CL}}$  as  $-298.66 \pm 0.03$  eV. Therefore, the valence band offset at the SiN<sub>x</sub>/Si interface is determined as  $-1.30 \pm 0.08$  eV and  $-1.29 \pm 0.08$  eV after degradation.

The optical bandgap determined immediately after film growth did not show a considerable difference to the aged bandgap. The conduction band offset at the interface prior to film alteration can therefore be determined as  $1.56 \pm 0.13$  eV and  $1.57 \pm 0.13$  eV, suggesting  $\Delta E_C/\Delta E_V$  as  $1.20 \pm 0.17$  and  $1.22 \pm 0.18$ . This implies that the hole-selectivity degrades.

Changes in the chemical composition of these films were investigated. The relative atomic concentrations of the elements in both freshly grown and aged 25 nm thick SiN<sub>x</sub> film were determined from CL peaks (Si 2*p*, N 1*s*, O 1*s*, and C 1*s*) taken from survey scans at multiple milling depths. These were fitted and corrected using their corresponding sensitivity factors, taking the mean free path of the photoelectrons and photoionization cross sections of these CLs into

account.<sup>38,39</sup> Survey identification and chemical state analysis techniques were used to investigate the chemical composition of this film. These are shown in Fig. 7. Based on the ion current density, sputter yield, and film density, the etch rate of this film using Ar ions was estimated to be  $\sim 0.20$  nm/s. When the thickness of the film is accurately known, etching beyond the interface using the Ar gun to identify the point at which there is a sudden drop of N concentration (in the substrate) further validates this etch rate.

The relatively high concentration of carbon and oxygen at the surface is likely due to organic contaminants and hydroxyl groups, respectively. The carbon concentration is considered to be negligible beyond the surface for both cases, while the presence of oxygen beyond the surface, as shown to be between 9% and 5% from a 4 nm to 16 nm depth, remains in the aged film. The concentration of oxygen is seen to be higher at all milling depths when compared to the as-deposited case, suggesting a transition to a more oxygen-rich film with aging. Furthermore, chemical state analysis using the ALSCOF library gives some indication of the film transitioning from silicon nitride to silicon oxy-nitride, based on the concentration levels detected. If only silicon nitride is considered, a 1:1 ratio between Si and N is observed beyond the surface.

The precursor used (BTBAS) is known to be capable of growing silicon oxy-nitride, as well as silicon nitride with various concentration ratios, depending on the growth conditions.<sup>40</sup> Initial work with the atomic concentration ratios of the freshly grown films shows a considerably lower oxygen concentration by 5%–7%, suggesting a transition to a more oxygen-rich film with aging. This could be the cause of the thickness and band offset shifts observed with aging. Increases in film thickness will reduce the conductivity of a passivating contact, but this could be mitigated by growing a thinner initial film. Decreases in band offset ratio (and so hole-selectivity) would be detrimental to the performance of a passivating contact, but it is encouraging that  $\Delta E_C/\Delta E_V$  remains greater than 1, even after aging. An assessment of the passivation, carrier tunneling, and selectivity properties of these ultrathin dielectrics will be reported in a follow-up study. Here, the potential of  $\text{SiN}_x$  nanofilms to act as

selective contacts is presented using specific contact resistivity ( $\rho_c$ ) measurements as well as analytical calculations and device simulations.

#### D. Specific contact resistivity of silicon nitride nanolayers

Maintaining a low  $\rho_c$  is a crucial factor for pursuing high performance carrier-selective contacts. In essence,  $\rho_c$  is a quantitative metric that characterizes the passage of electrical current through a carrier-selective contact. To measure  $\rho_c$  of an Ohmic contact, the Cox and Strack method (CSM) and transfer length method (TLM) are generally used.<sup>41–43</sup> These methods rely on using the current-voltage characteristics to extract the resistivity of the contact. The TLM technique measures the resistance via current flow only in the inversion layer of the contact, whereas current flows vertically in the CSM technique [as shown in Fig. 8(a)] under an applied voltage. The CSM technique is advantageous as the current distributes homogeneously below the contact rather than distributing exponentially directly below the contact as in the TLM technique. Nonetheless, in cases where hole transport materials and substrates are Schottky heterojunctions rather than Ohmic, the traditional approaches fail to accurately extract  $\rho_c$  due to rectification effects.<sup>44</sup> To tackle this, an expanded CSM technique that can effectively separate the contact resistivity from Schottky contacts has been reported and successfully used.<sup>44</sup> This combines the traditional CSM approach with Cheung's method to extract an effective  $\rho_c$ <sup>44–46</sup> and is used in our work.

As shown in Fig. 8(a), current flows longitudinally in the device under a varied applied voltage. From Fig. 8(a), the total resistance,  $R_T$ , is comprised of

$$R_T = R_C + R_S + R_O, \quad (3)$$

where  $R_C$  is the contact resistance,  $R_S$  is the spreading resistance in the substrate, and  $R_O$  is the residual resistance. The spreading resistance is defined as

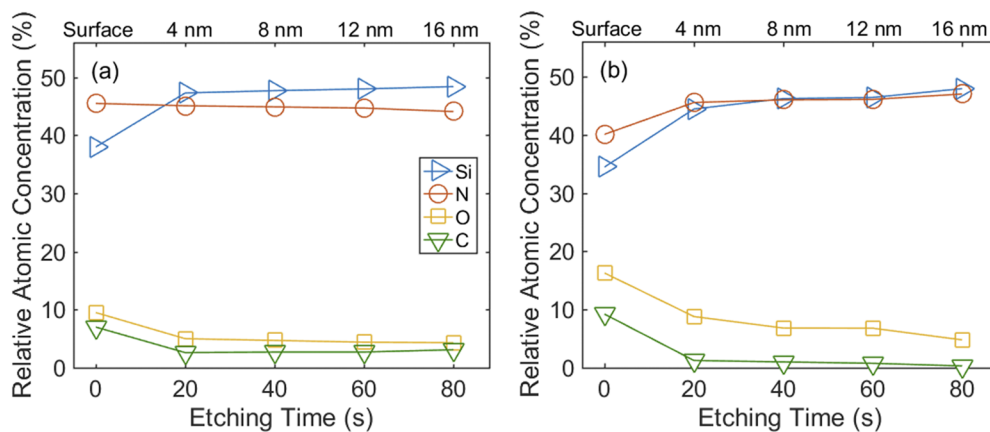


**FIG. 7.** Relative atomic concentration ratio of Si, N, O, and C as a function of etching time (corresponding to depth into the film) in the (a) as-deposited and (b) aged  $\text{SiN}_x$  bulk (25 nm thick film). Chemical state analysis was conducted using relative atomic sensitivity factors to fit the CLs of interest.

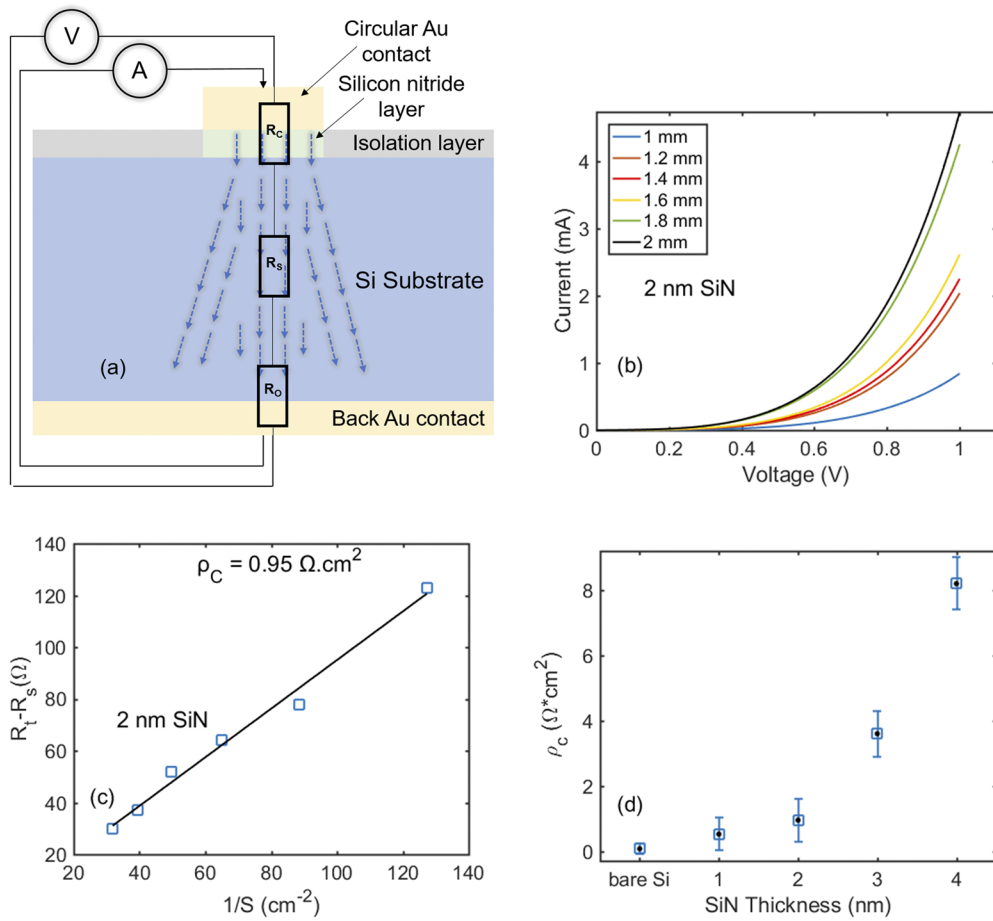


**FIG. 8.** (a) Cross-sectional diagram of fabricated Au/SiN<sub>x</sub>/Si/Au for CSM measurements, (b) current–voltage characteristics from the 2 nm SiN<sub>x</sub> thickness structure, (c)  $R_T - R_S$  vs  $1/S$  from the 2 nm SiN<sub>x</sub> thickness CSM structure and (d) dependency of  $\rho_c$  on SiN<sub>x</sub> thickness.

$$R_S = \frac{\rho}{d\pi} \arctan \frac{4t}{d}, \quad (4)$$

where  $d$  is the diameter of the circular electrode and  $\rho$  and  $t$  are the resistivity and thickness of the substrate, respectively. The contact resistance is defined as

$$R_C = \frac{\rho_c}{\pi d^2/4}. \quad (5)$$

To eradicate the rectification effects from the current–voltage characteristics of potential non-Ohmic contacts, we can extract  $R_T$  by combining the traditional CSM approach with<sup>44</sup>

$$\frac{d(V)}{d(\ln(I))} = R_T I + \frac{nq}{kT}, \quad (6)$$

where  $I$  is the current,  $V$  is the voltage,  $n$  is the ideality factor of the substrate,  $q$  is the electrical charge,  $k$  is the Boltzmann constant, and  $T$  is the temperature. The current–voltage characteristics with varying top electrode diameters between 1 mm and 2 mm are shown in Fig. 8(b). From the current–voltage characteristics,  $R_T$  is

determined by using Eq. (6) [ $\frac{d(V)}{d(\ln(I))}$  vs  $I$ ]. Following this,  $R_S$  and  $R_C$  are calculated using Eqs. (4) and (3), respectively. Consequently, we can determine  $\rho_c$ , by plotting  $R_C$  (where  $R_C = R_T - R_S$ ) against  $1/S$  (where  $S = \pi d^2/4$ ) and extracting the gradient. Figure 8(c) shows this plot for a 2 nm SiN<sub>x</sub> tunneling layer. In Fig. 8(d),  $\rho_c$  is shown as a function of SiN<sub>x</sub> thickness between 1 nm and 4 nm.

Using a SiN<sub>x</sub> thickness of 1 nm,  $\rho_c$  as low as  $0.52 \Omega \text{ cm}^2$  is achieved. This was found to increase up to  $0.95 \Omega \text{ cm}^2$ ,  $3.6 \Omega \text{ cm}^2$ , and  $8.2 \Omega \text{ cm}^2$  when using a SiN<sub>x</sub> layer thickness of 2 nm, 3 nm, and 4 nm, respectively. The general trend between increasing dielectric layer thickness resulting in a higher  $\rho_c$  in this type of contact is re-emphasized. The dependency of  $\rho_c$  on dielectric tunneling layer thickness is generally a trade-off between other contact quality metrics such as carrier lifetime.

To promote hole-selectivity and avoid Schottky barrier formation, multiple mechanisms can be used. First, a dielectric tunneling layer can be used that when interfaced with silicon, achieves favorable band alignments, which promotes majority carrier transport from the substrate to the external circuit. Another way is to use a

large work function metal that exceeds the work function of the silicon substrate, promoting upward band bending. A third way is to modulate the surface carrier concentration to further promote hole transport. This can be achieved using a material with a large fixed positive charge density, as typically done in (p)TOPCon with *p*-type polycrystalline silicon. Using analytical calculations and device simulations, we now look at the probability of hole tunneling at similar SiN<sub>x</sub> thicknesses shown in Fig. 8, with direct comparisons to TOPCon.

### E. Silicon nitride nanolayers as hole-selective contacts

Thin film passivating contacts are dependent on current transport through what would classically be considered insulators. While there is a debate on the exact nature of current transport through the dielectric film, it is generally accepted that tunneling plays a significant role for layers <2 nm.<sup>47–49</sup> Using the Wentzel–Kramers–Brillouin (WKB) approximation, the tunneling probability of carriers depends strongly on the barrier height ( $\Delta\phi_b$  given in eV), effective mass,  $m^*$ , and the dielectric thickness,  $t$ . This dependency is described by Eq. (7)<sup>50</sup> for the carrier tunneling probability,  $P_t$ ,

$$P_t = \exp\left(\frac{2}{\hbar} t \sqrt{2m^* q \Delta\phi_b}\right). \quad (7)$$

The intrinsic carrier selectivity of the dielectric,  $S_h$ , can be calculated as the ratio of the tunneling probability of holes to the tunneling probability of electrons,<sup>51</sup>

$$S_h = P_{t,h}/P_{t,e}. \quad (8)$$

To calculate the tunneling probabilities in SiO<sub>2</sub>, the conduction band barrier  $\Delta E_C$  was set to 3.2 eV, while the valence band barrier  $\Delta E_V$  was 4.7 eV.<sup>52</sup> The effective masses for electrons and holes were set to 0.4 and 0.58, respectively.<sup>52,53</sup> As the effective masses have a direct effect on the tunneling probability and current, a more detailed analysis of this parameter is provided in the [supplementary material](#). The band alignment found in this work was used for calculations

in SiN<sub>x</sub>, with  $\Delta E_C = 1.77$  eV and  $\Delta E_V = 1.09$  eV. For SiN<sub>x</sub>, the electron and hole effective masses were both set to 0.5.<sup>54</sup> The band offset values are visualized in Fig. 9(a), highlighting the smaller bandgap of SiN<sub>x</sub> compared to SiO<sub>2</sub>, and the band alignment of the dielectric in relation to a crystalline silicon absorber. Figure 9(b) compares the tunneling probability and selectivity of SiO<sub>2</sub> and (as-deposited) SiN<sub>x</sub>. The SiN<sub>x</sub> has larger hole tunneling probabilities for all thicknesses due to the smaller valence band offset, and it clearly favors hole tunneling as opposed to the electron-selective SiO<sub>2</sub>.

For a hole tunneling probability of  $10^{-8}$ , a SiN<sub>x</sub> layer of ~2.4 nm is required providing 150 times more hole tunneling than electron tunneling. A probability of  $10^{-8}$  is equivalent to that of electrons in a typical 1.4 nm SiO<sub>2</sub> for (n)TOPCon devices.<sup>55–57</sup> For an SiO<sub>2</sub> layer to achieve a similar hole tunneling probability, a 1.1 nm layer would be required, which exhibits preferential electron tunneling. This highlights the benefits of SiN<sub>x</sub> for hole-selective contacts. The exact values presented here depend on the effective masses used for the calculation. Despite the  $m^*$  used, the SiN<sub>x</sub> layer is still seen to outperform oxides in terms of hole tunneling. The reader is referred to the analysis included in the [supplementary material](#) for further details.

Sentaurus TCAD simulations were conducted to elucidate the effect that tunneling probability has in the current transfer dynamics across SiN<sub>x</sub> nanolayers. Tunneling across the dielectrics was simulated using Sentaurus's nonlocal tunneling model that implements Schenk and Heiser's approach,<sup>58</sup> with the extensions in Refs. 59 and 60. Mobility was modeled using Klaassen's mobility model,<sup>61,62</sup> while Schenk's low injection model was used for bandgap narrowing.<sup>63</sup> In passivated contacts, a highly doped poly silicon layer is often deposited on the tunneling dielectric layer, with the metal contact deposited last, as illustrated in Fig. 10(a). The wafer resistivity was set to 1  $\Omega$  cm, the poly Si doping density to  $6 \times 10^{19}$  cm<sup>-3</sup>, and a diffusion of Boron acceptors was set at the surface of the wafer with a 0.15  $\mu$ m depth factor using a Gaussian profile. Figures 10(b) and 10(c) compare the tunneling current for the selected thicknesses of as-deposited SiN<sub>x</sub> and SiO<sub>2</sub>, respectively.

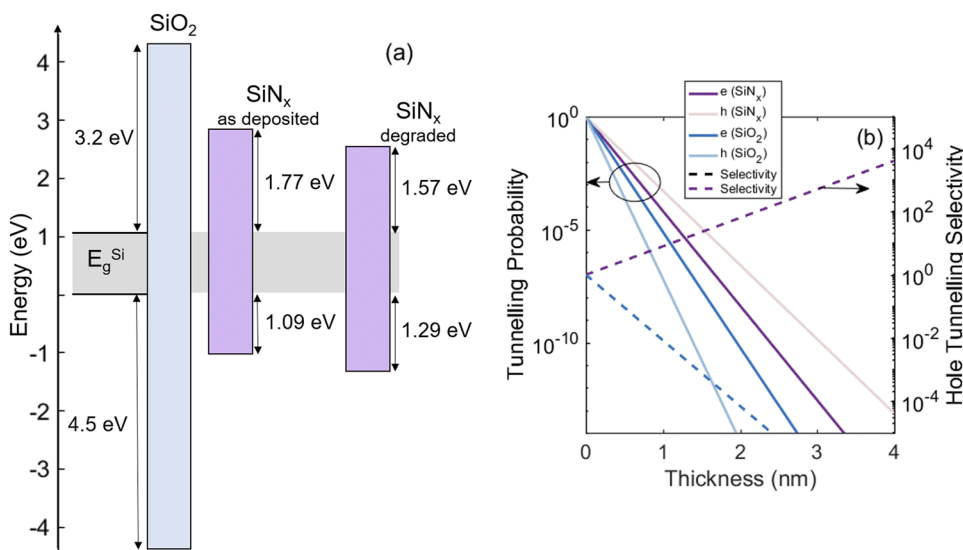


**FIG. 9.** (a) Measured  $\Delta E_C$  and  $\Delta E_V$  of SiN<sub>x</sub> compared to that of SiO<sub>2</sub>, and (b) tunneling probability and tunneling selectivity of as-deposited ALD SiN<sub>x</sub> and SiO<sub>2</sub>.

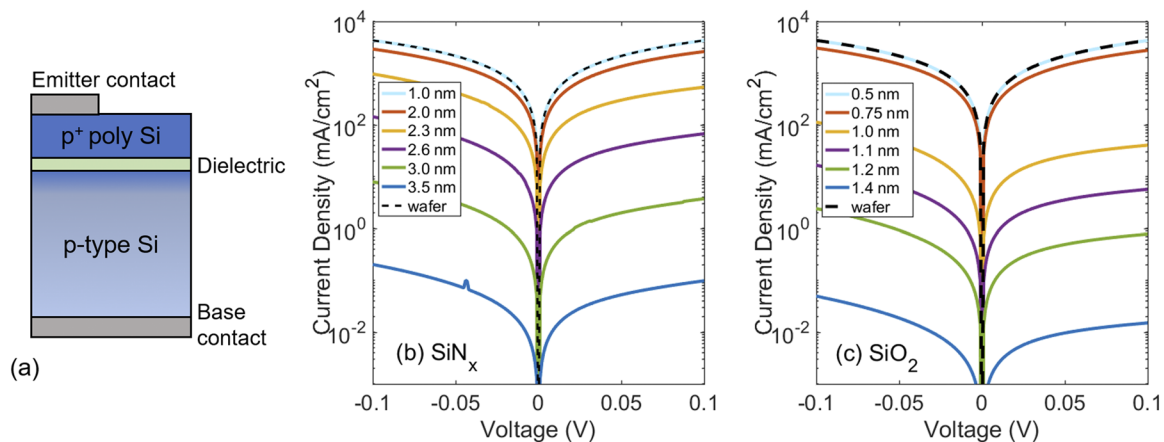


**FIG. 10.** (a) Schematic of the structure used in Sentaurus simulations. Tunneling current of (b) as-deposited ALD SiN<sub>x</sub> and (c) SiO<sub>2</sub>.

The curves show that, for a device with a SiN<sub>x</sub> nanolayer, the current is limited by the resistivity of the base when the thickness is below 2 nm. In a hole tunneling SiO<sub>2</sub> structure, the layer thickness must be under 0.7 nm for the total resistance to be limited by the base. Considering other values reported for  $m^*$  in SiO<sub>2</sub>, the limiting thickness increases to 1.1 nm. Still substantially thinner than that of a nitride nanolayer. In Fig. 10, it is also evident that the hole current density depends more strongly in the SiO<sub>2</sub> thickness than in the case of SiN<sub>x</sub>. Figures 10(b) and 10(c) show current densities spanning four orders of magnitude. In the SiN<sub>x</sub> structure, a thickness of 2.2 nm produces an industrially practical contact resistance of 100 mΩ cm<sup>2</sup>. Implementing an equivalent contact with SiO<sub>2</sub> would require a 1 nm nanolayer. This highlights a key advantage of SiN<sub>x</sub> as the film thickness does not require as rigorous control as for SiO<sub>2</sub>. From Figs. 9 and 10, it is clear that the favorable band alignment of SiN<sub>x</sub> translates into high hole tunneling current and high selectivity in the contact structures. Using ALD to deposit SiN<sub>x</sub> gives extremely accurate control of thicknesses, allowing the structures to be tailored to maximize the selectivity, while maintaining sufficient current.

#### IV. CONCLUSION

We show a highly controllable, Å-scale growth of SiN<sub>x</sub> films using atomic layer deposition and explore their hole-selectivity using a photoemission-based method to determine the band alignments at the SiN<sub>x</sub>/Si interface. The film thicknesses determined immediately after growth are seen to rise by 2 Å–5 Å over a period of 48 h after which the thickness stabilizes. A band offset ratio ( $\Delta E_C/\Delta E_V$ ) of  $1.62 \pm 0.24$  is determined for freshly grown samples. However, the hole-selectivity reduces during aging with a final  $\Delta E_C/\Delta E_V$  value of  $1.22 \pm 0.18$ . Despite the reduction in band offset ratio, a larger barrier to electrons than to holes remains, and therefore, these films show promise for applications in hole-selective contacts for silicon solar cells. A specific contact resistivity as low as 0.52 Ω cm<sup>2</sup> is achieved with sub-2 nm SiN<sub>x</sub> layers. Calculations of tunneling probability and selectivity of ALD SiN<sub>x</sub> are shown to demonstrate this potential. SiN<sub>x</sub> exhibits greater tunneling probability for holes than electrons, which results in a favorable hole-selectivity. In comparison to SiO<sub>2</sub>,

greater tunneling probabilities are calculated, which corresponds to higher current densities in the structure. Future studies will investigate the effective masses, passivation, and contacting quality of this material to further assess its suitability for fabricating hole-selective contacts for high-efficiency PV applications.

#### SUPPLEMENTARY MATERIAL

See the [supplementary material](#) for the consideration of carrier effective mass on tunneling, further discussion of the TCAD simulation parameters, and the XPS spectra for the aged SiN<sub>x</sub>/Si specimen.

#### ACKNOWLEDGMENTS

This work was supported by the Centre for Doctoral Training in New and Sustainable Photovoltaics (Grant No. EP/L01551X/1), the Supergen Solar Network+ (Grant No. EP/S000763/1), and Black Silicon Photovoltaics (Grant No. EP/R005303/1). R.S.B., a recipient of a Royal Academy of Engineering Research Fellowship, acknowledges the support from the EPSRC Postdoctoral Fellowship (Grant No. EP/M022196/1).

#### DATA AVAILABILITY

The data that support the findings of this study are available from the corresponding author upon reasonable request.

#### REFERENCES

- <sup>1</sup>International Energy Agency, Data & Statistics, <https://www.iea.org/subscribe-to-data-services/electricity-statistics>; accessed March 8, 2020.
- <sup>2</sup>G. Li, Z. Li, X. Liang, C. Guo, K. Shen, and Y. Mai, *ACS Appl. Mater. Interfaces* **11**, 828 (2019).
- <sup>3</sup>A. Richter, M. Hermle, and S. W. Glunz, *IEEE J. Photovoltaics* **3**, 1184 (2013).
- <sup>4</sup>B. Min, M. Müller, H. Wagner, G. Fischer, R. Brendel, P. P. Altermatt, and H. Neuhaus, *IEEE J. Photovoltaics* **7**, 1541 (2017).
- <sup>5</sup>K. Yoshikawa, W. Yoshida, T. Irie, H. Kawasaki, K. Konishi, H. Ishibashi, T. Asatani, D. Adachi, M. Kanematsu, H. Uzu, and K. Yamamoto, *Sol. Energy Mater. Sol. Cells* **173**, 37 (2017).

- <sup>6</sup>X. Zhu, *Acc. Chem. Res.* **46**, 1239 (2013).
- <sup>7</sup>K. Masuko, M. Shigematsu, T. Hashiguchi, D. Fujishima, M. Kai, N. Yoshimura, T. Yamaguchi, Y. Ichihashi, T. Mishima, N. Matsubara, T. Yamanishi, T. Takahama, M. Taguchi, E. Maruyama, and S. Okamoto, *IEEE J. Photovoltaics* **4**, 1433 (2014).
- <sup>8</sup>S. W. Glunz, F. Feldmann, A. Richter, M. Bivour, C. Reichel, H. Steinkemper, J. Benick, and M. Hermle, in *Photovoltaic Solar Energy Conference and Exhibition*, September 2015.
- <sup>9</sup>T. G. Allen, J. Bullock, X. Yang, A. Javey, and S. De Wolf, *Nat. Energy* **4**, 914 (2019).
- <sup>10</sup>J. Melskens, B. W. H. Van De Loo, B. Macco, L. E. Black, S. Smit, and W. M. M. Kessels, *IEEE J. Photovoltaics* **8**, 373 (2018).
- <sup>11</sup>Z. Wang, P. Li, Z. Liu, J. Fan, X. Qian, J. He, S. Peng, D. He, M. Li, and P. Gao, *APL Mater.* **7**, 110701 (2019).
- <sup>12</sup>F. Feldmann, M. Simon, M. Bivour, C. Reichel, M. Hermle, and S. W. Glunz, *Appl. Phys. Lett.* **104**, 181105 (2014).
- <sup>13</sup>A. Ingenito, G. Nogay, Q. Jeangros, E. Rucavado, C. Allebé, S. Eswara, N. Valle, T. Wirtz, J. Horzel, T. Koida, M. Morales-Masis, M. Despeisse, F.-J. Haug, P. Löper, and C. Ballif, *Nat. Energy* **3**, 800 (2018).
- <sup>14</sup>J. Stuckelberger, G. Nogay, P. Wyss, M. Lehmann, C. Allebe, F. Debrot, M. Ledinsky, A. Feifar, M. Despeisse, F. J. Haug, P. Loper, and C. A. Ballif, in *IEEE 43rd Photovoltaic Specialists Conference (PVSC)* (IEEE, 2016), p. 2518.
- <sup>15</sup>W. Yoon, J. E. Moore, E. Cho, D. Scheiman, N. A. Kotulak, E. Cleveland, Y.-W. Ok, P. P. Jenkins, A. Rohatgi, and R. J. Walters, *Jpn. J. Appl. Phys., Part 1* **56**, 08MB18 (2017).
- <sup>16</sup>R. Islam, P. Ramesh, J. H. Nam, and K. C. Saraswat, in *IEEE 42nd Photovoltaic Specialist Conference (PVSC)* (IEEE, 2015).
- <sup>17</sup>R. S. Bonilla, B. Hoex, P. Hamer, and P. R. Wilshaw, *Phys. Status Solidi A* **214**, 1700293 (2017).
- <sup>18</sup>H. Y. Wu, C. H. Hsu, T. X. Liu, Y. C. Ou, Y. H. Hsu, W. Y. Wu, S. Y. Lien, and Y. L. Jiang, *Surf. Coatings Technol.* **376**, 68 (2018).
- <sup>19</sup>Y. Wan, K. R. McIntosh, and A. F. Thomson, *AIP Adv.* **3**, 032113 (2013).
- <sup>20</sup>Y. Wan, K. R. McIntosh, A. F. Thomson, and A. Cuevas, in *Conference Record of the Twenty Sixth IEEE Photovoltaic Specialists* (IEEE, 2012), Vol. 3, p. 554.
- <sup>21</sup>A. G. Aberle, *Sol. Energy Mater. Sol. Cells* **65**, 239 (2001).
- <sup>22</sup>J. Robertson, *J. Vac. Sci. Technol., B* **18**, 1785 (2000).
- <sup>23</sup>F. Feldmann, M. Bivour, C. Reichel, H. Steinkemper, M. Hermle, and S. W. Glunz, *Sol. Energy Mater. Sol. Cells* **131**, 46 (2014).
- <sup>24</sup>S. Dauwe, L. Mittelstädt, A. Metz, and R. Hezel, *Prog. Photovoltaics Res. Appl.* **10**, 271 (2002).
- <sup>25</sup>H. C. M. Knoops, E. M. J. Braeken, K. De Peuter, S. E. Potts, S. Haukka, V. Pore, and W. M. M. Kessels, *ACS Appl. Mater. Interfaces* **7**, 19857 (2015).
- <sup>26</sup>M. Çopuroğlu, H. Sezen, R. L. Opila, and S. Suzer, *ACS Appl. Mater. Interfaces* **5**, 5875 (2013).
- <sup>27</sup>H. Konno, in *Materials Science and Engineering of Carbon* (Tsinghua University Press Limited, 2016), p. 8.
- <sup>28</sup>E. A. Kraut, R. W. Grant, J. R. Waldrop, and S. P. Kowalczyk, *Phys. Rev. Lett.* **44**, 1620 (1980).
- <sup>29</sup>E. A. Kraut, R. W. Grant, J. R. Waldrop, and S. P. Kowalczyk, *Phys. Rev. B* **28**, 1965 (1983).
- <sup>30</sup>S. A. Chambers, Y. Liang, Z. Yu, R. Droopad, J. Ramdani, and K. Eisenbeiser, *Appl. Phys. Lett.* **77**, 1662 (2000).
- <sup>31</sup>X. Lou, X. Gong, J. Feng, and R. Gordon, *ACS Appl. Mater. Interfaces* **11**, 28515 (2019).
- <sup>32</sup>T. Zhang, M. A. Hossain, C.-Y. Lee, Y. Zakaria, A. A. Abdallah, and B. Hoex, *Appl. Phys. Lett.* **113**, 262102 (2018).
- <sup>33</sup>B. Yan, S. Liu, Y. Heng, Y. Yang, Y. Yu, and K. Wen, *Nanoscale Res. Lett.* **12**, 363 (2017).
- <sup>34</sup>J. Tauc, in *The optical properties of solids* (Academic Press, 1966), p. 2.
- <sup>35</sup>R. K. Sonker, S. R. Sabhajeet, and B. C. Yadav, *J. Mater. Sci.: Mater. Electron.* **27**, 11726 (2016).
- <sup>36</sup>S. Jung, D. Gong, and J. Yi, *Sol. Energy Mater. Sol. Cells* **95**, 546 (2011).
- <sup>37</sup>M. Lynch, in *Proceedings of the Irish Machine Vision and Image Processing Conference (IMVIP)*, 2004, p. 04.
- <sup>38</sup>S. Tanuma, C. J. Powell, and D. R. Penn, *Surf. Interface Anal.* **21**, 165 (1994).
- <sup>39</sup>J. H. Scofield, *J. Electron Spectrosc. Relat. Phenom.* **8**, 129 (1976).
- <sup>40</sup>R. Laxman, D. Roberts, and A. K. Hochberg, U.S. patent 5,976,991 (15 December 1999).
- <sup>41</sup>R. H. Cox and H. Strack, *Solid-State Electron.* **10**, 1213 (1967).
- <sup>42</sup>W. Shockley, A. Goetzberger, and R. M. Scarlett, Report No. AFAL-TDR-64-207, AF Avionics, Wright-Patterson Air Force Base, OH, 1964, see <https://apps.dtic.mil/dtic/tr/fulltext/u2/605376.pdf>.
- <sup>43</sup>J. Bullock, Y. Wan, M. Hettick, J. Geissbuhler, A. J. Ong, D. Kiriya, D. Yan, T. Allen, J. Peng, X. Zhang, C. M. Sutter-Fella, S. De Wolf, C. A. Ballif, A. Cuevas, and A. Javey, in *Conference Record of the Twenty Sixth IEEE Photovoltaic Specialists* (IEEE, 2016), Vol. 16, p. 210.
- <sup>44</sup>W. Wang, H. Lin, Z. Yang, Z. Wang, J. Wang, L. Zhang, M. Liao, Y. Zeng, P. Gao, B. Yan, and J. Ye, *IEEE J. Photovoltaics* **9**, 1113 (2019).
- <sup>45</sup>G.-J. A. H. Wetzelaer, M. Scheepers, A. M. Sempere, C. Momblona, J. Ávila, and H. J. Bolink, *Adv. Mater.* **27**, 1837 (2015).
- <sup>46</sup>Y. Zhang, W. Cui, Y. Zhu, F. Zu, L. Liao, S.-T. Lee, and B. Sun, *Energy Environ. Sci.* **8**, 297 (2015).
- <sup>47</sup>A. Campa, F. Smole, N. Folchert, T. Wietler, B. Min, R. Brendel, and M. Topic, *IEEE J. Photovoltaics* **9**, 1575 (2019).
- <sup>48</sup>A. S. Kale, W. Nemeth, S. U. Nanayakkara, H. Guthrey, M. Page, M. Al-Jassim, S. Agarwal, and P. Stradins, in *IEEE 7th World Conference on Photovoltaic Energy Conversion (WCPEC)* (IEEE, 2018), p. 3473.
- <sup>49</sup>Y. Liu, P. Stradins, H. Deng, J. Luo, and S.-H. Wei, *Appl. Phys. Lett.* **108**, 022101 (2016).
- <sup>50</sup>H. C. De Graaff and J. G. De Groot, *IEEE Trans. Electron Devices* **26**, 1771 (1979).
- <sup>51</sup>S. Choi, K. H. Min, M. S. Jeong, J. I. Lee, M. G. Kang, H. E. Song, Y. Kang, H. S. Lee, D. Kim, and K. H. Kim, *Sci. Rep.* **7**, 12853 (2017).
- <sup>52</sup>A. Gehring and S. Selberherr, *IEEE Trans. Device Mater. Reliab.* **4**, 306 (2004).
- <sup>53</sup>R. K. Chanana, *J. Appl. Phys.* **109**, 104508 (2011).
- <sup>54</sup>A. V. Shaposhnikov, I. P. Petrov, V. A. Gritsenko, and C. W. Kim, *Phys. Solid State* **49**, 1628 (2007).
- <sup>55</sup>A. Moldovan, F. Feldmann, M. Zimmer, J. Rentsch, J. Benick, and M. Hermle, *Sol. Energy Mater. Sol. Cells* **142**, 123 (2015).
- <sup>56</sup>F. Feldmann, M. Bivour, C. Reichel, M. Hermle, and S. W. Glunz, *Sol. Energy Mater. Sol. Cells* **120**, 270 (2014).
- <sup>57</sup>A. S. Kale, W. Nemeth, S. P. Harvey, M. Page, D. L. Young, S. Agarwal, and P. Stradins, *Sol. Energy Mater. Sol. Cells* **185**, 270 (2018).
- <sup>58</sup>A. Schenk and G. Heiser, *J. Appl. Phys.* **81**, 7900 (1997).
- <sup>59</sup>F. Li, S. P. Mudanai, Y. Y. Fan, L. F. Register, and S. K. Banerjee, in *Device Research Conference - Conference Digest* (IEEE, 2003), Vol. 03, p. 47.
- <sup>60</sup>M. K. Jeong, P. M. Solomon, S. E. Laux, H. S. P. Wong, and D. Chidambarrao, in *IEEE Technical Digest - International Electron Devices Meeting* (IEEE, 1998), Vol. 98, p. 733.
- <sup>61</sup>D. B. M. Klaassen, *Solid-State Electron.* **35**, 953 (1992).
- <sup>62</sup>D. B. M. Klaassen, J. W. Slotboom, and H. C. de Graaf, *Solid-State Electron.* **35**, 125 (1992).
- <sup>63</sup>A. Schenk, *J. Appl. Phys.* **84**, 3684 (1998).